Published on 22 August 2018. Downloaded by Korea Institute of Science and Technology / KIST on 9/28/2018 1:29:03 AM.

Nanoscale

ROYAL SOCIETY OF CHEMISTRY

PAPER

View Article Online
View Journal | View Issue

Cite this: *Nanoscale*, 2018, **10**, 17712

Low-temperature wafer-scale synthesis of two-dimensional SnS_2†

Jung Joon Pyeon,[a,b] In-Hwan Baek,[a,c] Weon Cheol Lim,[d] Keun Hwa Chae,[d] Seong Ho Han,[e] Ga Yeon Lee,[e] Seung-Hyub Baek,[a] Jin-Sang Kim,[a] Ji-Won Choi,[a] Taek-Mo Chung,[e] Jeong Hwan Han,[f] Chong-Yun Kang[a,b] and Seong Keun Kim *[a]

Received 6th July 2018,
Accepted 21st August 2018

DOI: 10.1039/c8nr05450a

rsc.li/nanoscale

Research on two-dimensional (2D) metal dichalcogenides is rapidly expanding owing to their unique characteristics that do not exist in bulk materials. The industrially compatible development of these emerging materials is indispensable to facilitate the transition of 2D metal dichalcogenides from the research stage to the practical industrial application stage. However, an industrially relevant method, *i.e.*, the low-temperature synthesis of wafer-scale, continuous, and orientation-controlled 2D metal dichalcogenides, still remains a significant challenge. Here, we report the low-temperature (≲350 °C) synthesis of uniform and continuous n-type SnS_2 thin films *via* the combination of atomic layer deposition (ALD) of tin oxides and subsequent sulfurization. Well-crystallized and aligned SnS_2 layers parallel to the substrate are demonstrated through the phase engineering of the ALD-grown tin oxide and the substrate surface. The additional H_2S plasma treatment at 300 °C leads to the formation of stoichiometric SnS_2. The formation of conformal SnS_2 layers over a three-dimensional undulating hole structure is confirmed, which reveals the potential for applications beyond the planar structured architecture. The present results could be a step toward the realization of 2D metal dichalcogenides in industry.

Introduction

The technical demands on existing commercial devices far outstrip their current performance, necessitating significant innovation in the technologies that yield new device architectures and/or new materials. Two-dimensional (2D) metal dichalcogenides such as MoS_2 and WS_2 have unique electrical and optical properties and hence attract tremendous interest as new materials for a variety of applications, including transistors, sensors, and photodetectors.[1–6] Besides exploring the prospective functions of the materials, the development of industrially relevant growth techniques is essential to realize the potential of 2D metal dichalcogenides in emerging devices. From the perspective of technical application, the growth technique should provide excellent uniformity and a full coverage on a large scale. A low process temperature (≪500 °C) is critical for the integration of the materials in devices. Furthermore, the conformal growth of 2D metal dichalcogenides on a complex structure would help realize three-dimensional (3D) integrated devices.

Various growth methods have been proposed to date for the synthesis of 2D metal dichalcogenides. In particular, chemical vapor deposition (CVD) has been introduced to form well-crystallized films comprising grains with sizes of several tens of micrometers.[7,8] However, the CVD of continuous films on a large-area has been rarely reported.[9,10] In principle, the structural properties and spatial uniformity of CVD-grown 2D metal dichalcogenides are extremely sensitive to thermodynamic parameters, including the growth temperature and precursor concentration. The process adopted for the batch production of 2D metal dichalcogenides should be tolerant to fluctuations in the thermodynamic parameters. The extremely narrow window in the CVD process for the synthesis of 2D metal dichalcogenides is an obstacle in industrial applications. In addition, CVD requires a high temperature (>700 °C) for high crystallinity and effective control of the nucleation kinetics, which is not industrially feasible.

[a]*Center for Electronic Materials, Korea Institute of Science and Technology, Seoul 02792, Korea. E-mail: s.k.kim@kist.re.kr*
[b]*KU-KIST Graduate School of Converging Science and Technology, Korea University, Seoul 02841, Korea*
[c]*Department of Materials Science and Engineering, and Inter-University Semiconductor Research Center, Seoul National University, Seoul 08826, Korea*
[d]*Advanced Analysis Center, Korea Institute of Science and Technology, Seoul 02792, Korea*
[e]*Division of Advanced Materials, Korea Research Institute of Chemical Technology, Daejeon 34114, Korea*
[f]*Department of Materials Science and Engineering, Seoul National University of Science and Technology, Seoul 01811, Korea*

†Electronic supplementary information (ESI) available. See DOI: 10.1039/c8nr05450a

 This journal is © The Royal Society of Chemistry 2018

Published on 22 August 2018. Downloaded by Korea Institute of Science and Technology / KIST on 9/28/2018 1:29:03 AM.

The abovementioned two challenges—poor process tolerance and high process temperature—must be addressed *via* two different approaches based on modification of the processes and materials. Growth techniques based on a self-limiting mechanism are desirable for the synthesis of 2D metal dichalcogenides. In particular, atomic layer deposition (ALD), a representative technique based on the self-limiting mechanism, has wide tolerance for thermodynamic parameters such as the vapor pressure of the precursors. Hence, the direct ALD growth of layered materials or sulfurization of ALD-grown oxides is advantageous for full coverage growth and spatial uniformity in the film thickness, as well as the grain size of 2D metal dichalcogenides on a wafer-scale area. Materials with a low melting point (T_m) are favorable for lowering the growth temperature. In this regard, SnS_2 is worthy of consideration because its T_m (869 °C)[11] is substantially lower than that of representative 2D metal dichalcogenides such as MoS_2 (T_m: 1185 °C) and WS_2 (T_m: 1250 °C). Such a low T_m of SnS_2 enables the direct growth of high quality SnS_2 on a substrate without a transfer process.

SnS_2 is an intrinsic n-type layered semiconductor similar to MoS_2. Its reported bandgap (2.1–2.77 eV)[7,12,13] is significantly larger than that of MoS_2, which allows for clear switching (high on/off current ratio) in thin-film transistor (TFT) applications. The electron mobility in SnS_2 is ~230 cm^2 V^{-1} s^{-1},[14] which is comparable to that (>200 cm^2 V^{-1} s^{-1})[1] in MoS_2. In addition, the electron affinity in SnS_2 is larger than that in MoS_2;[15,16] therefore, SnS_2 enables true Ohmic conduction in junctions with source/drain electrodes. SnS_2 shows performance comparable to that of MoS_2 in a variety of applications such as TFTs,[17,18] photodetectors,[19] and sensors.[20]

Here, we report a wafer-scale synthesis of continuous SnS_2 layers by sulfurization combined with the ALD of tin oxides. The overall process was executed under a stringent thermal limit of ≤350 °C. Such a low process temperature and the wafer-scale uniformity of SnS_2 validate the industrial compatibility of this sulfurization. Herein, the critical features of this process, including the chemical composition, orientation preference, and morphology evolution, are systematically studied. We demonstrate that oxide phases such as SnO_2 and SnO determine the sulfurization kinetics, and that the substrate surface is a considerable factor for the morphology engineering of SnS_2. The good conformality on the 3D hole structure shows the potential for the application of 2D SnS_2 in 3D integrated devices. The results of these systematic sulfurization studies would contribute to advances in the synthesis of other 2D materials as well as SnS_2.

Results and discussion

1. Synthesis and wafer level homogeneity of single-phase SnS_2

The overall synthesis of large-area SnS_2 thin films is illustrated in Fig. 1a. Prior to the deposition of tin oxides, two surfaces—amorphous SiO_2 and Al_2O_3—with different surface energies were prepared as the substrates. Two different phases, SnO_2 and SnO were used as mother materials, and both oxide films were grown by ALD. The thickness of the tin oxides was controlled by the change in the number of ALD cycles to vary the thickness of SnS_2. Subsequently, both SnO_2 and SnO thin films were sulfurized under an Ar/H_2S (3.5%) atmosphere at a low temperature of 350 °C. For further improvement, the sulfurized films were treated under Ar/H_2S (3.5%) plasma at 300 °C. It is noteworthy that all the processes were performed at low temperatures (≤350 °C), which is compatible with the conventional fabrication processes for electronic devices.

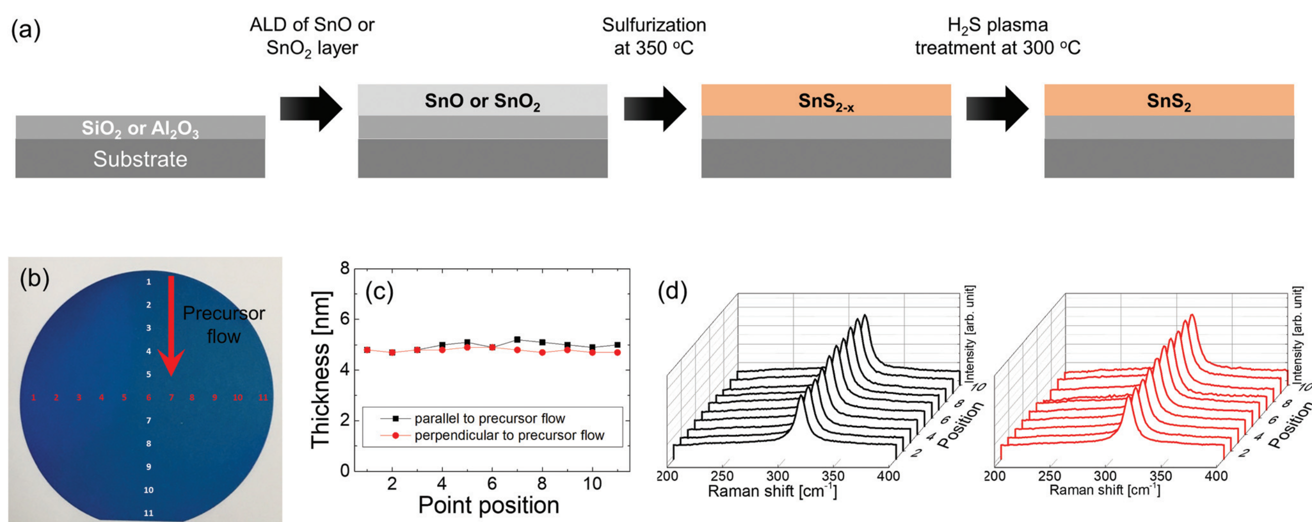

Fig. 1 Synthesis of SnS_2 and its wafer-scale homogeneity. (a) Schematic illustration of the synthesis procedure of 2D SnS_2. (b) Photograph of the SnS_2 film formed on a four-inch $Al_2O_3/SiO_2/Si$ wafer by the aforesaid procedure. (c) Variation in the film thickness measured at positions indicated in b. (d) Raman spectra of the SnS_2 obtained at positions indicated in b (left: parallel to precursor flow, right: perpendicular to precursor flow).

Published on 22 August 2018. Downloaded by Korea Institute of Science and Technology / KIST on 9/28/2018 1:29:03 AM.

In addition to process temperature compatibility, the large-area growth with excellent uniformity in physical and chemical properties is another critical factor affecting the widespread application of 2D metal dichalcogenides in industry. Fig. 1b shows the photograph of the SnS_2 film formed on a four-inch $Al_2O_3/SiO_2/Si$ wafer *via* the process illustrated in Fig. 1a. The thicknesses of the SnS_2 films on the wafer were measured by spectroscopic ellipsometry along the directions parallel and perpendicular to the precursor flow (Fig. 1c). The average thickness measured on all the points was 4.9 nm, and the standard deviation was as low as 0.15 nm. The SnS_2 film thickness can be controlled by the variation in the number of SnO ALD cycles. The film thickness of SnS_2 has a strong linear relationship with the thickness of SnO (Fig. S1†). To further examine the structural uniformity, Raman spectra were obtained from several positions on the four-inch wafer indicated in Fig. 1b (Fig. 1d). All the Raman spectra show only a characteristic peak at 314 cm^{-1} corresponding to a SnS_2 A_{1g} Raman mode.[13] The intensities of the characteristic SnS_2 A_{1g} Raman mode are similar, irrespective of the measuring position. The negligible fluctuation reflects the excellent structural homogeneity of SnS_2, suggesting that the proposed sulfurization combined with the ALD process enables the uniform growth of a single-phase SnS_2 with large scalability.

The excellent uniformity over a large area results from the following two features of this method. In principle, ALD, which is based on the self-limiting mechanism, is advantageous in terms of uniformity over a large area. The excellent uniformity of the ALD-grown tin oxides allows for the good uniformity of the sulfurized layer. In addition, the sulfurization process is self-limiting. The thermodynamic calculation shown in Fig. 2a indicates that the sulfurization of Al_2O_3 and SiO_2 used as the substrates is not possible under the current conditions. The sulfurization of tin oxides terminates when the SnO or SnO_2 layer is completely consumed. This suggests that within a sufficient sulfurization time, the fluctuation of thermodynamic parameters, such as the local deviation of H_2S vapor pressure, has no notable influence on the film homogeneity.

2. Sulfurization of tin oxides: SnO_2 *vs.* SnO

Oxide sulfurization proceeds by the diffusion of the sulfur reactant into the sulfurized layer, and the chemical reaction between the sulfur reactant and the oxide at the sulfide/oxide interface. It is noteworthy that various tin oxide phases such as SnO_2 and SnO exist. The plausible reactions of SnO and SnO_2 with H_2S are shown below:

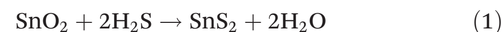

$$SnO_2 + 2H_2S \rightarrow SnS_2 + 2H_2O \quad (1)$$

$$SnO + 2H_2S \rightarrow SnS_2 + H_2O + H_2 \quad (2)$$

Both the chemical reactions have negative Gibbs free energies in the entire temperature range of 300–900 K (Fig. 2a), confirming that these oxides are spontaneously sulfurized under the present conditions.

However, the chemical reactivity at the SnS_2/oxide interface is determined by the type of tin oxide phase. The different chemical reactivities influence the sulfurization and the pro-

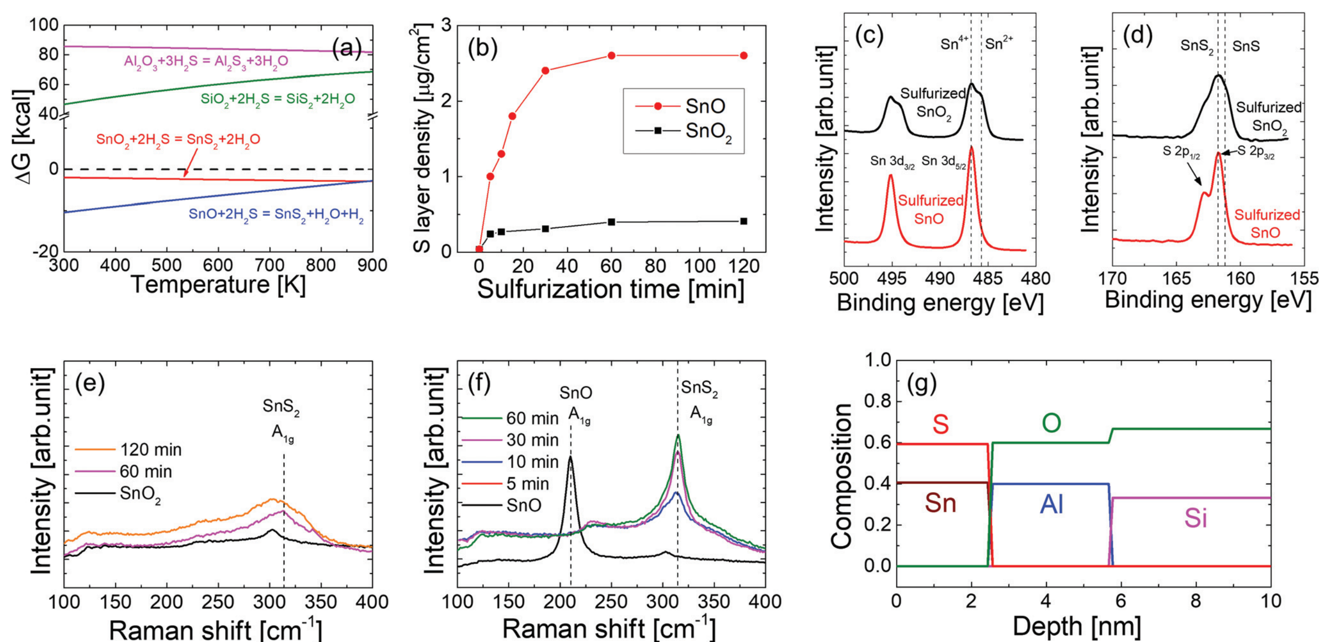

Fig. 2 Comparison of sulfurization properties of ALD-grown SnO and SnO_2. (a) Standard Gibbs free energies for reactions of SnO, SnO_2, Al_2O_3 and SiO_2 with H_2S as a function of temperature. (b) Variation in the layer density of S ions in the SnO and SnO_2 films sulfurized at 350 °C as a function of the sulfurization time. X-ray photoelectron spectra of (c) Sn 3d and (d) S 2p core levels in the SnO_2 and SnO thin films sulfurized at 350 °C for 60 min, respectively. Raman spectra of the (e) SnO_2 and (f) SnO thin films sulfurized at 350 °C, respectively. (g) The MEIS depth profile of the chemical composition of the 3 nm thick SnO sulfurized at 350 °C.

This journal is © The Royal Society of Chemistry 2018

Published on 22 August 2018. Downloaded by Korea Institute of Science and Technology / KIST on 9/28/2018 1:29:03 AM.

perties of the sulfurized layer. Hence, the sulfurization of both SnO and SnO_2 films was examined. We confirmed that the SnO and SnO_2 films were each formed in a single phase by ALD (Fig. S2†). Fig. 2b shows the variation in the layer density of S ions in the films sulfurized at 350 °C as a function of the sulfurization time. The layer density of S ions in Fig. 2b represents the amount of tin sulfides formed. Here, the amounts of Sn ions in both SnO (layer density of Sn: 6.8 μg cm^{-2}) and SnO_2 (layer density of Sn: 7.2 μg cm^{-2}) films were almost identical to each other, thus making the thickness of the sulfides formed from SnO and SnO_2 after full sulfurization identical. The thicknesses of the SnO and SnO_2 films were 6.4 nm and 9.8 nm, respectively. Although the layer density of S ions in both SnO and SnO_2 films increased with the sulfurization time, a large difference in the amounts of the sulfurized layer was observed. When the sulfurization time exceeded 60 min, the layer density of S ions in the sulfurized SnO saturated to approximately 2.6 μg cm^{-2} because of the complete consumption of SnO, as will be discussed later. The layer density of S ions in the sulfurized SnO_2 was only 0.4 μg cm^{-2} even at a long sulfurization time of 120 min. The amount of Sn in SnO and SnO_2 did not change during sulfurization (Fig. S3†), indicating that the low S content in the sulfurized SnO_2 is not due to material volatilization.

The chemical binding states of the sulfurized layers were examined by X-ray photoelectron spectroscopy (XPS). Fig. 2c and d shows the X-ray photoelectron spectra of (c) Sn 3d and (d) S 2p core levels in the SnO and SnO_2 thin films sulfurized at 350 °C for 60 min, respectively. The Sn 3d spectrum of the sulfurized SnO thin film showed a single Sn $3d_{5/2}$ peak at 486.7 eV corresponding to a Sn oxidation state of +4. The peak at 485.7 eV corresponding to a Sn oxidation state of +2, which was observed in the spectrum of the pristine SnO film, disappeared. In the S 2p spectrum of the sulfurized SnO thin film, two peaks were observed at 161.8 eV and 162.9 eV, corresponding to the S $2p_{3/2}$ and S $2p_{1/2}$ peaks of SnS_2, respectively. A valley between the two peaks was clearly observed, and there was no peak corresponding to SnS. In the sulfurization-processed SnO_2, which was much less sulfurized as seen in Fig. 2b, two Sn $3d_{5/2}$ peaks could be observed at 486.7 eV and 485.7 eV corresponding to Sn oxidation states of +4 and +2, respectively (Fig. 2c). The existence of two different sulfide phases, SnS (161.2 eV (ref. 21)) and SnS_2 (161.8 eV), was also verified in the S 2p spectrum of the sulfurized SnO_2.

Raman analysis of the sulfurized SnO and SnO_2 also revealed that the former is a better mother material for the synthesis of SnS_2. Fig. 2e and f shows the Raman spectra of the sulfurized SnO_2 and SnO thin films, respectively. The sulfurized SnO_2 gave a broad and weak peak at 314 cm^{-1} corresponding to the characteristic A_{1g} mode of SnS_2[13] despite the long sulfurization time of 120 min, whereas the sulfurized SnO films showed a distinct Raman A_{1g} mode of SnS_2. The intensity of the characteristic A_{1g} mode was significantly enhanced as the sulfurization time increased up to 60 min. These results suggested that the chemical reactivity of SnO with H_2S is higher than that of SnO_2 with H_2S and that only a single phase of SnS_2 is formed by the sulfurization of SnO. In other words, SnO is highly favorable for the synthesis of SnS_2 at low temperatures.

The chemical composition of the sulfurized SnO along the film thickness was examined using medium energy ion scattering (MEIS) (Fig. 2g and Fig. S4†). The oxygen content in the sulfurized layer was negligible. This observation supported the fact that the sulfurization of SnO beyond a certain time (Fig. 2b) was terminated because of the complete consumption of SnO. In addition, the MEIS depth profile showed a very sharp interface between the sulfurized layer and Al_2O_3 because of the improbability of sulfurization of Al_2O_3 under the current conditions. However, the S/Sn atomic ratio of the sulfurized SnO was approximately 1.5, which is below the stoichiometric value of SnS_2. As shown in Fig. 2b, the non-stoichiometry of the film could not be improved by a further increase in the sulfurization time. The improvement in the sulfur content of the films will be discussed later.

3. Influence of the substrate from the perspective of surface energy

Here, we investigate the influence of the substrate on the morphology evolution of SnS_2 formed by the sulfurization of SnO. SnO thin films were grown on both amorphous SiO_2 and Al_2O_3 surfaces under the same conditions. The properties of the SnO thin films were almost similar, irrespective of the substrate (Fig. S5†). Fig. 3a and b shows the atomic force microscopy (AFM) images of the SnO thin films grown on the Al_2O_3 and SiO_2 substrates, respectively. Both films had a smooth surface, with a root-mean-squared (RMS) roughness of approximately 1 nm. No distinct difference in the film surface could be observed in the two cases. After sulfurization at 350 °C, however, a significant change in the surface morphology was observed. The sulfurized SnO film on the Al_2O_3 substrate displayed a similar morphology to the pristine SnO film, and the RMS roughness increased slightly to about 1.2 nm (Fig. 3c). Meanwhile, the surface of the sulfurized SnO film on the SiO_2 substrate was not homogeneous, and island-like grains were found (Fig. 3d). Considering that the properties of the SnO films on the Al_2O_3 and SiO_2 substrates were similar, the substrate might be a decisive factor in the surface morphology change of the sulfurized films.

SnS_2 has strong anisotropy, and its surface energy is reported to be 540 mJ m^{-2} for the (100) plane and 104 mJ m^{-2} for the (001) plane.[22] As compared to the basal plane of SnS_2, an amorphous SiO_2 surface has a lower surface energy (40–80 mJ m^{-2}),[23–25] while an amorphous Al_2O_3 surface has high surface energy (700–1000 mJ m^{-2}).[26,27] This trend in the surface energy of the substrates used in this work was also verified by contact angle measurements (Fig. S6†). The amorphous Al_2O_3 substrate exhibited a smaller contact angle than did the SiO_2 substrate, indicating that the Al_2O_3 surface has a higher surface energy than does the SiO_2 surface.

The morphology evolution of thin films is determined to minimize the surface free energy of the films. The surface energy of the amorphous Al_2O_3 was higher than that of the

Published on 22 August 2018. Downloaded by Korea Institute of Science and Technology / KIST on 9/28/2018 1:29:03 AM.

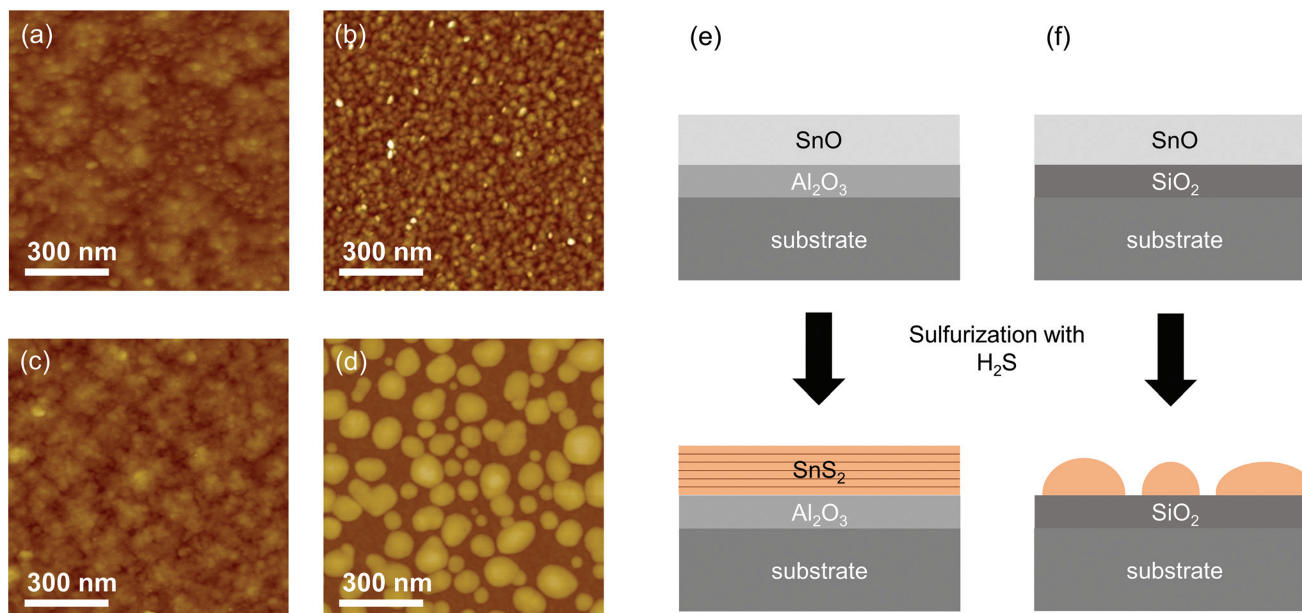

Fig. 3 Morphology evolution of SnS_2 depending on the substrate surface. AFM images of the ALD-grown SnO on (a) amorphous Al_2O_3 and (b) SiO_2 substrates and the sulfurized SnO on (c) amorphous Al_2O_3 and (d) SiO_2 substrates. Schematic illustration for sulfurization of SnO on the (e) Al_2O_3 substrate with high surface energy and the (f) SiO_2 substrate with low surface energy.

SnS_2 (001) basal plane. Therefore, Al_2O_3 with high surface energy was fully covered with the sulfurized layer to minimize the surface energy (Fig. 3e). On the other hand, it would be favorable to expose the SiO_2 surface with low surface energy in the sulfurized layer/SiO_2 sample, so that islands could be formed *via* coalescence (Fig. 3f).

Facile atomic movement is required for the morphology evolution described in Fig. 3e and f. The sulfurization temperature in this work is low at 350 °C, which would not be sufficient for the facile atomic movement in the other sulfides and oxides because of the kinetic limit. However, the atomic movement is related to the reduced temperature (T/T_m) of the material, rather than the process temperature itself.[28] The T_m of SnS_2 is very low, *i.e.*, 869 °C. The reduced temperature of SnS_2 is as high as 0.55 at a sulfurization temperature of 350 °C, which enables coalescence (Fig. 3d). Therefore, the microstructure evolution is understood to be substrate-dependent; these results suggest that a high-surface-energy substrate such as amorphous Al_2O_3 is indispensable to form smooth and continuous SnS_2 films.

4. Plasma treatment for further improvement and necessity of two-step sulfurization

Although the sulfurization of SnO on Al_2O_3 substrates yields smooth, oxygen-free, and single-phase sulfide films, the issue of sulfur deficiency must be addressed. An additional treatment using H_2S plasma at a low temperature of 300 °C for 30 min was attempted for the formation of stoichiometric SnS_2 after sulfurization at 350 °C. Fig. 4a and b shows the Sn 3d and S 2p core-level X-ray photoelectron spectra of the sulfurized SnO/Al_2O_3 films before and after the H_2S plasma post-treatment, respectively. The core-level Sn 3d spectra of the films showed a negligible difference after the H_2S plasma post-treatment. The spectrum of the H_2S plasma-treated sample showed a S $2p_{3/2}$ peak at 161.8 eV, which was identical to that for the film before the H_2S plasma treatment. However, the intensity of the S 2p peak increased notably after the H_2S plasma post-treatment. The S/Sn atomic ratio of the H_2S plasma-treated film, as estimated from the peak area and relative sensitivity factors of Sn and S, was approximately 1.91, which is very close to the stoichiometric value. The variation in the S/Sn atomic ratio of the films was also verified by wavelength-dispersive X-ray fluorescence (WDXRF) analysis. Fig. 4c shows the variation in the S/Sn atomic ratio of the sulfurized films after the H_2S plasma post-treatment at 300 °C for 30 min. Although the S/Sn ratio of all the thermally sulfurized films remained below 1.5, the H_2S plasma post-treatment significantly increased the S/Sn ratio of the films. In particular, the S/Sn ratio of the sulfurized SnO above the S/Sn ratio of 1.3 saturated to 1.92 after the H_2S plasma post-treatment.

The H_2S plasma post-treatment does not change the surface morphology of the film (Fig. 4d). The peak intensity of the characteristic A_{1g} Raman mode of the sulfurized SnO/Al_2O_3 sample significantly increases after the H_2S plasma post-treatment (Fig. 4e). Fig. 4f shows the θ–2θ X-ray diffraction (XRD) patterns of the sulfurized SnO/Al_2O_3 samples before and after the H_2S plasma treatment. Peaks due to the SnS and Sn_2S_3 phases are not detected. Only the SnS_2 (001) peak is observed in the θ–2θ XRD patterns of both films, and the peak intensity also increases after the H_2S plasma post-treatment, indicating

 This journal is © The Royal Society of Chemistry 2018

Published on 22 August 2018. Downloaded by Korea Institute of Science and Technology / KIST on 9/28/2018 1:29:03 AM.

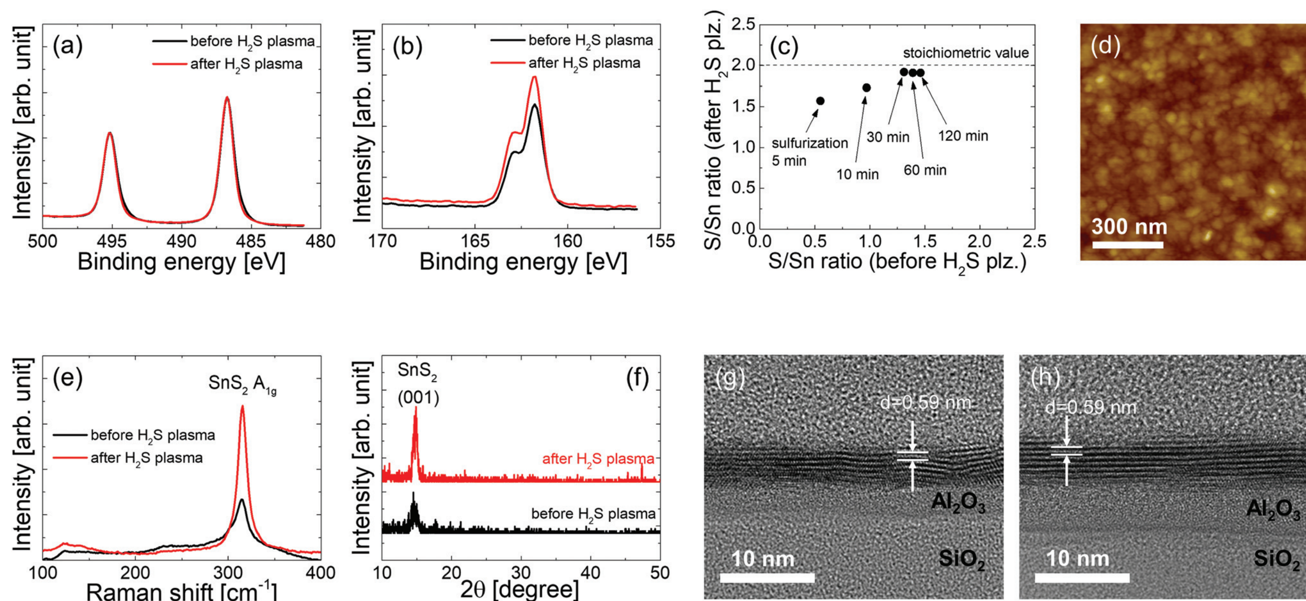

Fig. 4 Improvement in the properties of SnS_2 by the subsequent H_2S plasma treatment at 300 °C. X-ray photoelectron spectra of (a) Sn 3d and (b) S 2p core levels in the sulfurized $SnO/Al_2O_3/SiO_2/Si$ before and after the H_2S plasma treatment at 300 °C for 30 min. (c) Variation in the S/Sn ratio of the sulfurized SnO after the H_2S plasma treatment. (d) AFM image of the sulfurized SnO after the H_2S plasma treatment. (e) Raman spectra and (f) θ–2θ XRD patterns of the sulfurized SnO/Al_2O_3 samples before and after H_2S plasma post-treatment. Cross-section HRTEM images of the sulfurized SnO/Al_2O_3 samples (g) before and (h) after H_2S plasma treatment.

that the crystallinity of the film is improved and that the SnS_2 (001) plane is more aligned parallel to the substrate after the H_2S plasma post-treatment. Fig. 4g and h shows the cross-sectional high-resolution transmission electron microscopy (HRTEM) images of the sulfurized SnO/Al_2O_3 samples (g) before and (h) after the H_2S plasma post-treatment, respectively. The thermally sulfurized SnO/Al_2O_3 is crystallized; the plane with an interspacing of 0.59 nm corresponding to SnS_2 (001) is aligned in parallel to the substrate (Fig. 4g), consistent with the XRD results in Fig. 4f. However, the film consists of small SnS_2 grains (lateral size < 10 nm), and the basal plane of the grains is slightly misaligned. Through the H_2S plasma treatment, the slight misalignment of the basal plane is drastically improved, and the lateral size of the grains increases (Fig. 4h).

Bottom-gate TFTs with the SnS_2 layer as shown in Fig. 5a were fabricated to evaluate the electrical performance of the SnS_2 films. Fig. 5b and c displays the transfer curves of the TFTs with the 3 nm thick SnS_2 layer formed by (b) the only sulfurization at 350 °C and (c) two-step sulfurization, sulfurization at 350 °C and the subsequent H_2S plasma treatment at 300 °C, respectively. Both TFTs exhibit a typical n-type transistor behavior, supporting that the grown channel materials have an n-type nature. The on/off current ratio of the TFTs is approximately 10^3 for the only sulfurization-processed film and 10^5 for the two-step sulfurization-processed film, respectively. The off-current level for both TFTs is sufficiently low below 10^{-12} A. The difference in the on/off ratio for the TFTs is mainly due to the difference in the on-currents. The field effect mobility (μ_{FE}) is extracted from the transfer curves in Fig. 5b and c. The μ_{FE} can be expressed as

$$\mu_{FE} = \frac{L}{WC_{ox}V_{DS}} \times \frac{\Delta I_{DS}}{\Delta V_{GS}} \tag{3}$$

where L = 50 μm is the channel length, W = 300 μm is the channel width, C_{ox} is the capacitance of the gate dielectric composed of 4 nm thick Al_2O_3/100 nm thick SiO_2, V_{DS} is the drain–source voltage, I_{DS} is the drain–source current, and V_{GS} is the gate bias. The extracted μ_{FE} in the TFT with the only sulfurization-processed SnS_2 layer is as low as 2×10^{-4} cm^2 V^{-1} s^{-1}. Such a low value might result from the significant S deficiency and the small grain size. The TFT with the H_2S plasma post-treated SnS_2 has an extracted μ_{FE} of 0.02 cm^2 V^{-1} s^{-1}, and shows a two orders of magnitude increase in the on-current compared to the TFT with the thermally sulfurized SnO layer. These results demonstrate that the additional H_2S plasma treatment contributes to the formation of stoichiometric SnS_2 and the improvement in the crystallinity of the SnS_2 films.

In contrast to the properties of TFTs with MoS_2, a representative 2D dichalcogenide, that have been extensively reported, the electrical properties of TFT devices with SnS_2 have been rarely reported. A μ_{FE} of ≈1 cm^2 V^{-1} s^{-1} has been reported from an exfoliated SnS_2 [17] and the value of ≈2 cm^2 V^{-1} s^{-1} has been also reported from a CVD-grown SnS_2 flake.[13] Although these μ_{FE} values are larger than the obtained μ_{FE} in this work, those device properties are obtained from a single crystal flake, and not a continuous film of SnS_2. Choi *et al.* have recently reported the formation of the continuous SnS_2 layers

Published on 22 August 2018. Downloaded by Korea Institute of Science and Technology / KIST on 9/28/2018 1:29:03 AM.

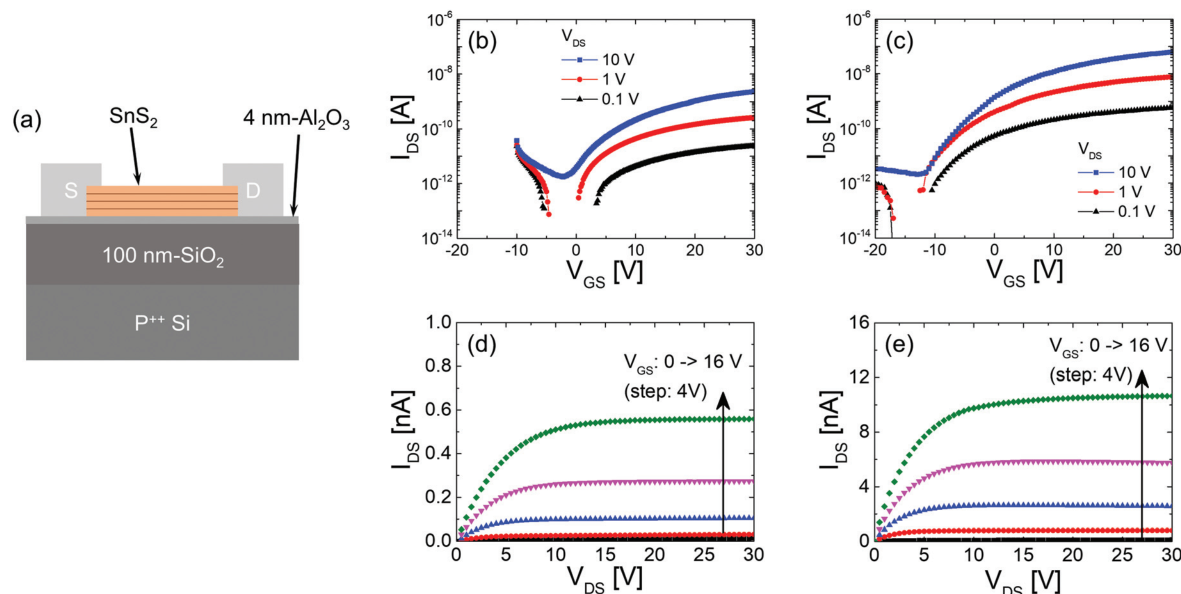

Fig. 5 Characteristics of TFT devices. (a) Schematic illustration of the bottom-gate TFT with SnS_2 as the channel layer. Transfer curves of the TFTs with the SnS_2 layer formed by (b) the only sulfurization at 350 °C and (c) the sulfurization followed by the H_2S plasma treatment at 300 °C, respectively. Output characteristics of the TFTs with the SnS_2 layer formed by (d) the only sulfurization at 350 °C and (e) the sulfurization followed by the H_2S plasma treatment at 300 °C, respectively.

formed *via* transformation of ALD-grown SnS by annealing at 450 °C and have obtained the TFT performances (on/off ratio: 2×10^3 and μ_{FE}: 0.014 $cm^2 V^{-1} s^{-1}$) of the continuous SnS_2 layers.[29] Despite the lower thermal limit of 350 °C, our TFTs show slightly better electrical performance compared to the TFTs in their report.

Both TFTs with the SnS_2 layers before and after H_2S plasma post-treatment also show a clear pinch-off in the output characteristics (Fig. 5d and e). I_{DS} is linearly proportional to V_{DS} in the low V_{DS} region for the TFTs, revealing an Ohmic conduction at source/drain contacts. This might result from the high work function of the SnS_2, which demonstrates that SnS_2 is free from the issues of a large contact resistance, which is a critical problem in MoS_2 TFTs.[30]

It is noteworthy that a single step sulfurization using H_2S plasma is not appropriate for the formation of single phase SnS_2. Fig. 6a shows the variations in the layer density of S ions and the S/Sn ratio in the 6.4 nm thick SnO films treated with H_2S plasma at 300 °C as a function of the treatment time. The layer density of S ions in the films saturates to ~1.5 μg cm^{-2} and the S/Sn ratio of the films remains approximately 0.8, which is far below the stoichiometric value. The sulfurized layer thickness in the SnO treated with H_2S plasma at 300 °C alone is found to be very limited due to the kinetic limit. Even at a higher temperature of 350 °C where the SnO layer was fully sulfurized under an H_2S atmosphere as shown in Fig. 2, the single step sulfurization using H_2S plasma does not produce a single phase of SnS_2. Fig. 6b shows Raman spectra of the SnO treated with H_2S plasma at 350 °C. Characteristic peaks corresponding to orthorhombic and cubic π SnS as well as SnS_2 are observed. Surprisingly, the peak intensity corresponding to SnS increases with the H_2S plasma sulfurization time. Zhang *et al.* have recently reported that H_2S is catalytically decomposed by SnS_2 with the formation of H_2 and the generated H_2 reduced SnS_2 to SnS at ≥350 °C.[31] The H_2S plasma contains the activated hydrogen as well and such activated hydrogen might reduce SnS_2 to SnS. In addition, the H_2S plasma treatment at 350 °C alone roughens the film surface (Fig. 6c–e). The scanning electron microscopy images in Fig. 6c–e indicate that the grains in the films sulfurized by the single step of H_2S plasma treatment at 350 °C are randomly oriented. Therefore, the two-step process, *i.e.*, the combination of sulfurization at a higher temperature and subsequent plasma treatment at a lower temperature, is necessary to form stoichiometric and continuous SnS_2 on a large area in an industrially compatible manner.

5. Conformality of SnS_2

The implementation of 2D metal chalcogenides in 3D structures holds great promise for a variety of applications. The critical requirements for application to 3D devices are thickness conformality and structural homogeneity of the 2D layers on a demanding substrate. The synthesis of approximately 3 nm thick SnS_2 is demonstrated over a 3D hole structure (Fig. 7). The conformal growth of crystallized SnS_2 is verified owing to the beneficial features of ALD. The direct ALD growth of other 2D materials has been also reported to achieve good conformality in physical thickness.[32,33] However, the preferential orientation of the layers was not well controlled, and randomly oriented flake-like grains were obtained.[32,34] Considering the strong anisotropy of 2D metal dichalcogenides, the alignment of the basal plane on more demanding

 This journal is © The Royal Society of Chemistry 2018

Published on 22 August 2018. Downloaded by Korea Institute of Science and Technology / KIST on 9/28/2018 1:29:03 AM.

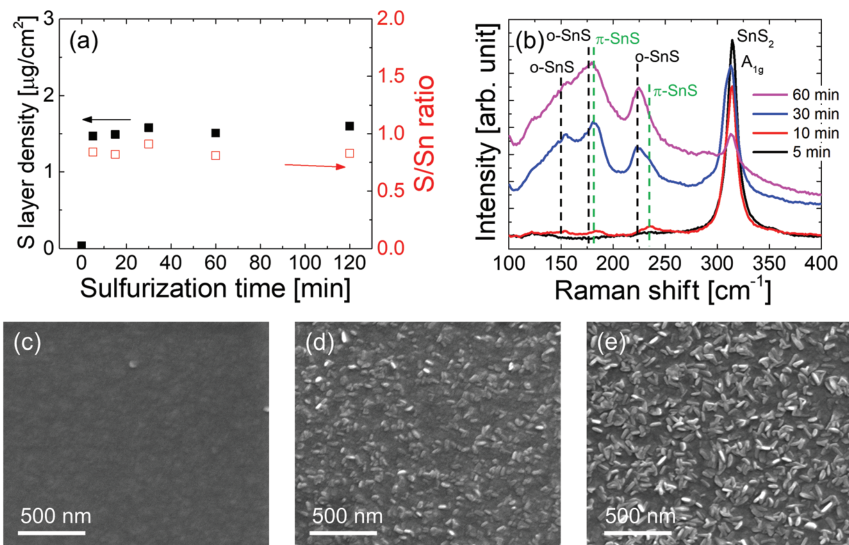

Fig. 6 Limitation of a single step sulfurization using H_2S plasma. (a) Variation in the S layer density and the S/Sn ratio of 6.4 nm thick SnO films treated with H_2S plasma at 300 °C. (b) Raman spectra of the SnO films treated with H_2S plasma at 350 °C (*o*-SnS: orthorhombic SnS and π-SnS: cubic SnS). Scanning electron microscopy images of the SnO films treated with H_2S plasma at 350 °C for (c) 5, (d) 10 and (e) 60 min, respectively.

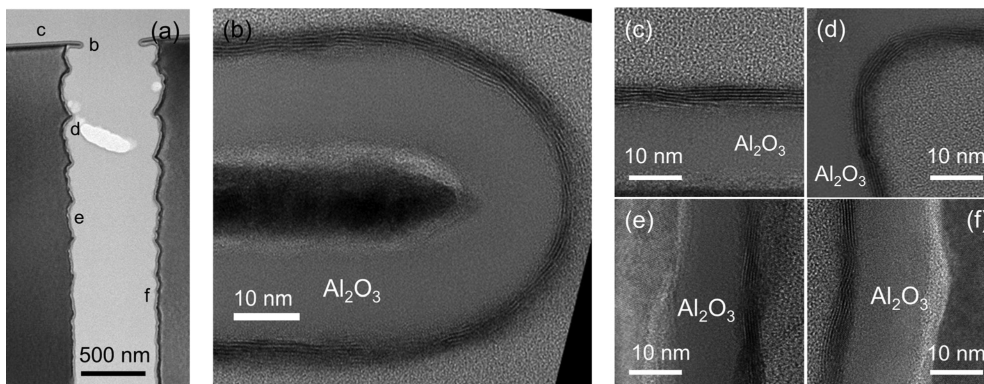

Fig. 7 Step coverage of SnS_2. (a) TEM image of the SnS_2 grown on a 3D undulating hole structure. (b)–(f) HRTEM images of SnS_2 at the positions indicated in a.

substrates is crucial in terms of uniformity of the properties. As shown in Fig. 7b–f, the (001) basal plane of SnS_2 is well developed along the undulating morphology resulting from the Bosch process. In particular, the basal plane of the SnS_2 is evolved parallel to the substrate surface even at an extremely small radius (~25 nm) of curvature (Fig. 7b). Therefore, the synthesis process proposed in this work can help realize 3D nanoelectronic devices based on 2D SnS_2.

Conclusions

We propose an industrially relevant synthesis of layer-structured SnS_2 *via* the sulfurization of ALD-grown tin oxides. Phase engineering of tin oxides as mother materials and the substrate surface leads to wafer-scale growth of uniform and continuous SnS_2 layers aligned parallel to the substrate at low temperatures (≤350 °C). The chemical reactivity of the oxide with H_2S at the SnS_2/tin oxide interface is significantly affected by the oxide phase. SnO is found to be more beneficial for the formation of SnS_2 at lower temperatures than is SnO_2. Full coverage of the films and preferential orientation of the basal plane parallel to the substrate surface are achieved on the Al_2O_3 substrate with higher surface energy. The subsequent H_2S plasma treatment at 300 °C reduces the sulfur deficiency and enhances the crystallinity of the SnS_2 films. The conformality benefit of ALD facilitates excellent step coverage of SnS_2 on the undulating hole structure. These results demonstrate that the industrially compatible low-temperature process would allow for the use of SnS_2 in emerging devices in mass production. Furthermore, the systematic study on the sulfurization of SnS_2 provides insight into advances in the sulfurization of other 2D materials. The sulfurization technique can be even expanded to atomically thin metal oxides from liquid

Published on 22 August 2018. Downloaded by Korea Institute of Science and Technology / KIST on 9/28/2018 1:29:03 AM.

metals[35–37] beyond ALD-grown oxides. We believe that this work would be an important step toward the incorporation of 2D metal chalcogenides in industry. For this purpose, the studies on various applications of the SnS_2 films are under investigation.

Experimental details

Formation of SnO and SnO_2 thin films

SnO thin films were deposited by ALD at 210 °C. Bis(1-dimethylamino-2-methyl-2-propoxy)tin(II), with an Sn valence state of +2, was used as the Sn precursor. H_2O vapor was used as the oxygen precursor. The detailed growth conditions for SnO ALD are reported elsewhere.[38,39] SnO_2 thin films were also deposited by ALD at 180 °C using tetrakis(dimethylamino)tin and H_2O as the Sn and oxygen precursors, respectively. A 100 nm thick thermally oxidized SiO_2/Si and a 4 nm thick Al_2O_3-coated SiO_2/Si were used as the substrates.

Sulfurization

SnO and SnO_2 thin films were sulfurized at 350 °C under an H_2S (3.5%)/Ar atmosphere for 5–120 min. Subsequent H_2S plasma treatment was performed at 300 °C for 30 min in the other chamber. H_2S plasma was produced by a flow of H_2S (3.5%)/Ar gas of 200 sccm at a radiofrequency power of 150 W.

Characterization

The thicknesses of the SnS_2 thin films were evaluated by spectroscopic ellipsometry. The layer density of Sn and S ions in the films was measured by WDXRF. Raman spectroscopy and XPS were utilized to observe the chemical states of the SnS_2 films. The surface morphology of the SnS_2 films was observed by AFM and scanning electron microscopy. The depth profile of the chemical composition of the SnS_2 film was examined using MEIS. Furthermore, the crystallinity and orientation preference of the films were studied by θ–2θ XRD and HRTEM.

Thin film transistor fabrication

We fabricated bottom-gate thin film transistors with the SnS_2 layer as an n-type channel. Heavily doped p-type Si served as the gate and 4 nm thick Al_2O_3/100 nm thick SiO_2 was used as the gate dielectric. The thickness of the SnS_2 was fixed at 3 nm and the channel was patterned by photolithography. The length and the width of the channel is 50 μm and 300 μm, respectively. 30 nm thick Ti/30 nm thick Au electrodes (source and drain) were grown by evaporation, respectively. The electrodes were deposited in the same chamber without breaking the vacuum.

Conflicts of interest

There are no conflicts to declare.

Acknowledgements

This work was supported by the Korea Institute of Science and Technology (KIST through 2E28210).

References

1 B. Radisavljevic, A. Radenovic, J. Brivio, V. Giacometti and A. Kis, *Nat. Nanotechnol.*, 2011, **6**, 147–150.
2 F. K. Perkins, A. L. Friedman, E. Cobas, P. M. Campbell, G. G. Jernigan and B. T. Jonker, *Nano Lett.*, 2013, **13**, 668–673.
3 A. Splendiani, L. Sun, Y. Zhang, T. Li, J. Kim, C.-Y. Chim, G. Galli and F. Wang, *Nano Lett.*, 2010, **10**, 1271–1275.
4 D. Lembke, S. Bertolazzi and A. Kis, *Acc. Chem. Res.*, 2015, **48**, 100–110.
5 D. Jariwala, V. K. Sangwan, L. J. Lauhon, T. J. Marks and M. C. Hersam, *ACS Nano*, 2014, **8**, 1102–1120.
6 C. Yang, X. Run, Y. Zhihao, P. Yiming, O. Zhun-Yong, W. Xiaoxu, W. Junzhuan, N. Haiyan, N. Zhenhua, W. Yun, C. Tangsheng, S. Yi, W. Baigeng, Z. Gang, Z. Yong-Wei and W. Xinran, *Adv. Mater.*, 2015, **27**, 5230–5234.
7 G. Ye, Y. Gong, S. Lei, Y. He, B. Li, X. Zhang, Z. Jin, L. Dong, J. Lou, R. Vajtai, W. Zhou and P. M. Ajayan, *Nano Res.*, 2017, **10**, 2386–2394.
8 J. Chen, W. Tang, B. Tian, B. Liu, X. Zhao, Y. Liu, T. Ren, W. Liu, D. Geng, H. Y. Jeong, H. S. Shin, W. Zhou and K. P. Loh, *Adv. Sci.*, 2016, **3**, 1600033.
9 H. Yu, M. Liao, W. Zhao, G. Liu, X. J. Zhou, Z. Wei, X. Xu, K. Liu, Z. Hu, K. Deng, S. Zhou, J.-A. Shi, L. Gu, C. Shen, T. Zhang, L. Du, L. Xie, J. Zhu, W. Chen, R. Yang, D. Shi and G. Zhang, *ACS Nano*, 2017, **11**, 12001–12007.
10 K. Kang, S. Xie, L. Huang, Y. Han, P. Huang, K. Mak, C.-J. Kim, D. Muller and J. Park, *Nature*, 2015, **520**, 656–660.
11 I. D. Olekseyuk, I. V. Dudchak and L. V. Piskach, *J. Alloys Compd.*, 2004, **368**, 135–143.
12 J. C. Park, K. R. Lee, H. Heo, S.-H. Kwon, J.-D. Kwon, M.-J. Lee, W. Jeon, S.-J. Jeong and J.-H. Ahn, *Cryst. Growth Des.*, 2016, **16**, 3884–3889.
13 J.-H. Ahn, M.-J. Lee, H. Heo, J. H. Sung, K. Kim, H. Hwang and M.-H. Jo, *Nano Lett.*, 2015, **15**, 3703–3708.
14 Y. Huang, E. Sutter, J. T. Sadowski, M. Cotlet, O. L. A. Monti, D. A. Racke, M. R. Neupane, D. Wickramaratne, R. K. Lake, B. A. Parkinson and P. Sutter, *ACS Nano*, 2014, **8**, 10743–10755.
15 F. A. Rasmussen and K. S. Thygesen, *J. Phys. Chem. C*, 2015, **119**, 13169–13183.
16 L. A. Burton, D. Colombara, R. D. Abellon, F. C. Grozema, L. M. Peter, T. J. Savenije, G. Dennler and A. Walsh, *Chem. Mater.*, 2013, **25**, 4908–4916.
17 D. Debtanu, M. John, S. Sean, Z. Vincent, G. Arnold and P. Haibing, *Nanotechnology*, 2013, **24**, 025202.

This journal is © The Royal Society of Chemistry 2018

Published on 22 August 2018. Downloaded by Korea Institute of Science and Technology / KIST on 9/28/2018 1:29:03 AM.

18 H. S. Song, S. L. Li, L. Gao, Y. Xu, K. Ueno, J. Tang, Y. B. Cheng and K. Tsukagoshi, *Nanoscale*, 2013, **5**, 9666–9670.

19 G. Su, V. G. Hadjiev, P. E. Loya, J. Zhang, S. Lei, S. Maharjan, P. Dong, P. M. Ajayan, J. Lou and H. Peng, *Nano Lett.*, 2015, **15**, 506–513.

20 J. Z. Ou, W. Ge, B. Carey, T. Daeneke, A. Rotbart, W. Shan, Y. Wang, Z. Fu, A. F. Chrimes, W. Wlodarski, S. P. Russo, Y. X. Li and K. Kalantar-zadeh, *ACS Nano*, 2015, **9**, 10313–10323.

21 I.-H. Baek, J. J. Pyeon, Y. G. Song, T.-M. Chung, H.-R. Kim, S.-H. Baek, J.-S. Kim, C.-Y. Kang, J.-W. Choi, C. S. Hwang, J. H. Han and S. K. Kim, *Chem. Mater.*, 2017, **29**, 8100–8110.

22 M. Li, E. Liu, H. Hu, S. Ouyang, H. Xu and D. Wang, *Int. J. Photoenergy*, 2014, **2014**, 7.

23 W.-Y. Chou, C.-W. Kuo, H.-L. Cheng, Y.-R. Chen, F.-C. Tang, F.-Y. Yang, D.-Y. Shu and C.-C. Liao, *Appl. Phys. Lett.*, 2006, **89**, 112126.

24 P. Miskiewicz, S. Kotarba, J. Jung, T. Marszalek, M. Mas-Torrent, E. Gomar-Nadal, D. B. Amabilino, C. Rovira, J. Veciana, W. Maniukiewicz and J. Ulanski, *J. Appl. Phys.*, 2008, **104**, 054509.

25 R. Hayakawa, M. Petit, T. Chikyow and Y. Wakayama, *Appl. Phys. Lett.*, 2008, **93**, 153301.

26 A. H. Tavakoli, P. S. Maram, S. J. Widgeon, J. Rufner, K. van Benthem, S. Ushakov, S. Sen and A. Navrotsky, *J. Phys. Chem. C*, 2013, **117**, 17123–17130.

27 A. A. Demkov and A. Navrotsky, *Thermodynamics of oxide systems relevant to alternative gate dielectrics*, Springer, Netherlands, 2005, ch. 3.

28 I. Petrov, P. B. Barna, L. Hultman and J. E. Greene, *J. Vac. Sci. Technol., A*, 2003, **21**, S117–S128.

29 H. Choi, J. Lee, S. Shin, J. Lee, S. Lee, H. Park, S. Kwon, N. Lee, M. Bang, S.-B. Lee and H. Jeon, *Nanotechnology*, 2018, **29**, 215201.

30 S. Das, H.-Y. Chen, A. V. Penumatcha and J. Appenzeller, *Nano Lett.*, 2013, **13**, 100–105.

31 H. Zhang, Y. Balaji, A. Nalin Mehta, M. Heyns, M. Caymax, I. Radu, W. Vandervorst and A. Delabie, *J. Mater. Chem. C*, 2018, **6**, 6172–6178.

32 J. Hämäläinen, M. Mattinen, K. Mizohata, K. Meinander, M. Vehkamäki, J. Räisänen, M. Ritala and M. Leskelä, *Adv. Mater.*, 2018, **30**, 1703622.

33 Y. Jang, S. Yeo, H.-B.-R. Lee, H. Kim and S.-H. Kim, *Appl. Surf. Sci.*, 2016, **365**, 160–165.

34 T. A. Ho, C. Bae, S. Lee, M. Kim, J. M. Montero-Moreno, J. H. Park and H. Shin, *Chem. Mater.*, 2017, **29**, 7604–7614.

35 A. Zavabeti, J. Z. Ou, B. J. Carey, N. Syed, R. Orrell-Trigg, E. L. H. Mayes, C. Xu, O. Kavehei, A. P. O'Mullane, R. B. Kaner, K. Kalantar-zadeh and T. Daeneke, *Science*, 2017, **358**, 332–335.

36 B. J. Carey, J. Z. Ou, R. M. Clark, K. J. Berean, A. Zavabeti, A. S. R. Chesman, S. P. Russo, D. W. M. Lau, Z.-Q. Xu, Q. Bao, O. Kavehei, B. C. Gibson, M. D. Dickey, R. B. Kaner, T. Daeneke and K. Kalantar-Zadeh, *Nat. Commun.*, 2017, **8**, 14482.

37 T. Daeneke, P. Atkin, R. Orrell-Trigg, A. Zavabeti, T. Ahmed, S. Walia, M. Liu, Y. Tachibana, M. Javaid, A. D. Greentree, S. P. Russo, R. B. Kaner and K. Kalantar-Zadeh, *ACS Nano*, 2017, **11**, 10974–10983.

38 S. H. Kim, I.-H. Baek, D. H. Kim, J. J. Pyeon, T.-M. Chung, S.-H. Baek, J.-S. Kim, J. H. Han and S. K. Kim, *J. Mater. Chem. C*, 2017, **5**, 3139–3145.

39 J. H. Han, Y. J. Chung, B. K. Park, S. K. Kim, H.-S. Kim, C. G. Kim and T.-M. Chung, *Chem. Mater.*, 2014, **26**, 6088–6091.